



COPY NO. 16

IMPACT DAMAGE IN CARBON-CARBON COMPOSITES

Technical Report

05/01/77 thru 10/31/77 Contract No. N00014-76-C-0854

> Project No. 471 (NR032-570)

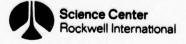
Submitted to:

Office of Naval Research 800 N. Quincy Street Arlington, VA 22217

Approved for Public Release; distribution unlimited

AD NO.

This Research was Sponsored by the Office of Naval Research Under Contract No. N00014-76-C-0854 (Project No. 471)





SECURITY CLASSIFICATION OF THIS PAGE (When Date Entered)

REPORT DOCUMENTATION PAGE	READ INSTRUCTIONS BEFORE COMPLETING FORM
1. REPORT NUMBER 2. GOVT ACCESSION NO	3. RECIPIENT'S CATALOG NUMBER
61	
TTLE (and Subtitle)	5. TYPE OF REPORT & PERIOD COVERED Technical
TIMACE DAMAGE TH CARRON CARRON COMPOSTERS	05/01/77 thru 10/31/77
IMPACT DAMAGE IN CARBON-CARBON COMPOSITES.	\
(14	6. PERFORMING ORG. REPORT NUMBER SC5076.4TR
AUTHOR(a)	8. CONTRACT OR GRANT NUMBER(s)
(15	NØ0014-76-C-Ø854
William F. Adler and Anthony G./Evans	
9. PERFORMING ORGANIZATION NAME AND ADDRESS	10. PROGRAM ELEMENT PROJECT, TASK
Rockwell International	10. PROGRAM ELEMENT, PROJECT, TASK AREA & WORK UNIT NUMBERS
Science Center	
Thousand Oaks, CA 91360	Project No. 471 (NRO32-570)
11. CONTROLLING OFFICE NAME AND ADDRESS	12. REPORT DATE
Office of Naval Research	November 11, 1977
800 N. Quincy Street	13. NUMBER OF PAGES
Arlington, VA 22217 (Code 471) 14. MONITORING AGENCY NAME & ADDRESS(II different from Controlling Office)	15. SECURITY CLASS. (of this report)
TO TO THE AGENCY NAME & ADDRESS, I WINDS HIM COMMON THE	G. SESSILL SEASE (S. MILE ISPON)
I technical rept.	Unclassified
1 May - 31 Oct 7%	15a. DECLASSIFICATION/DOWNGRADING
1 May - 51 00 15	SCHEDOLE
16. DISTRIBUTION STATEMENT (of this Report)	(12)0/
A	1/6P.
Approved for Public Release; distribution unlimi	ted
17. DISTRIBUTION STATEMENT (of the abstract entered in Block 20, if different to	rom Report)
18. SUPPLEMENTARY NOTES	
19. KEY WORDS (Continue on reverse side if necessary and identify by block number	
Carbon composites, impact, erosion, damage modes	
hypervelocity impact, penetration mechanics, sho	ck waves, stress waves.
/	
26. ABSTRACT (Continue on reverse side if necessary and identify by block number	
The damage to three-dimensional orthogonal carbon- particle impacts ranging from 1800 to 6000 ms had	
weave constructions at both ambient and at tempera	
subsurface damage modes in the vicinity of the imp	
the range of conditions investigated. Hypotheses	
failure modes and kinetics for the material eject	
examination of sectioned specimens and high-speed	
Penetration, compliance and plane-strain compress	ion tests are utilized to

389949

UNCLASSIFIED

UNCLASSIFIED
SECURITY CLASSIFICATION OF THIS PAGE(When Data Entered)

supply mechanical characterization data for the dominant modes of failure, which are analyzed in terms of the dynamic stress states which develop in the three-dimensional composites during the collision cycle.

ACCESSION MTIS	White Section
DDC	Buff Section
ENANNOUN	CED
JUSTIFICAT	101
B Y . ,	Cara ta a
DISTRIBUTI	ON/AVAILABILITY CODES
DISTRIBUTI	ON/AVAILABILITY CODES



IMPACT DAMAGE IN CARBON-CARBON COMPOSITES

TECHNICAL REPORT 05/01/77 thru 10/31/77

Submitted to:

Office of Naval Research 800 N. Quincy Street Arlington, VA 22217



TABLE OF CONTENTS

PART I:		EROSION DAMAGE IN CARBON-CARBON COMPOSITES AT HYPERSONIC IMPACT VELOCITIES	
			Page
1.0	1.0 INTRODUCTION		4
2.0		DAMAGE OBSERVATIONS	6
	2.1	DAMAGE PERSPECTIVES	6
	2.2	DAMAGE DETAILS	8
	2.3	MATERIAL EJECTION	9
3.0		QUASI-STATIC STUDIES	11
	3.1	PENETRATION TESTS	11
	3.2	COMPLIANCE TESTS	13
	3.3	PLANE-STRAIN COMPRESSION TESTS	13
4.0		DAMAGE ANALYSIS	16
	4.1	IMPACT STRESSES	16
	4.2	DAMAGE MECHANISMS	18
5.0		SUMMARY AND GENERAL IMPLICATIONS	20
		ACKNOWLEDGEMENTS	22
		REFERENCES	23
PART II:		A COMPRESSIONAL MODE OF DAMAGE IN CARBON COMPOSITES	
1.0		INTRODUCTION	1
2.0		DAMAGE OBSERVATIONS	1
3.0		DAMAGE ANALYSIS	2
4.0		DISCUSSION	7
		APPENDIX I	8
		FIGURE CAPTIONS	10
		REFERENCES	11



PART I

EROSION DAMAGE IN CARBON-CARBON COMPOSITES

AT HYPERSONIC IMPACT VELOCITIES

by

W. F. Adler and A. G. Evans



Erosion Damage in Carbon-Carbon Composites at Hypersonic Impact Velocities

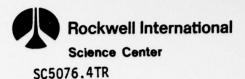
William F. Adler and Anthony G. Evans

Abstract

The damage to three-dimensional orthogonal carbon-carbon composites created by particle impacts ranging from 1800 to 6000 ms⁻¹ has been characterized for three weave constructions at both ambient and at temperatures up to 3600°C. The subsurface damage modes in the vicinity of the impact crater are described for the range of conditions investigated. Hypotheses are advanced concerning the failure modes and kinetics for the material ejected from the crater based on examination of sectioned specimens and high-speed photographic sequences. Penetration, compliance, and planestrain compression tests are utilized to supply mechanical characterization data for the dominant modes of failure, which are analyzed in terms of the dynamic stress states which develop in the three-dimensional composites during the collision cycle.

^{*}Director, Materials Science Section, Effects Technology, Inc., 5383
Hollister Ave., Santa Barbara, CA 93111.

Group Leader, Structural Ceramics, Structural Materials Department, Rockwell International Science Center, 1049 Camino Dos Rios, Thousand Oaks, CA 91360.

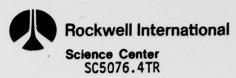


1.0 INTRODUCTION

Investigation of the erosive response of fibrous composites exposed to natural (rain/ice) and induced (dust) particulate environments is stimulated by the need for re-entry vehicle protection materials. The erosion performance of existing system materials has been evaluated using ground impact simulation testing and verification flight tests. (1-6) In the evaluation of materials fabricated for improved erosion resistance, all material evaluation has been directly related to erosion test performance. Little attention has been given to information for material development activities. It has thus been difficult for material manufacturers to relate erosion test results, such as mass loss ratios, to material construction or processing variables.

Mass loss determinations have been performed either by single particle impact procedures (6) or by continuous erosion testing in ballistic range facilities. (1-3) Mass loss laws have then been derived for specific materials based on experimental correlations. However, the single particle studies have not adequately represented effects of multiple collisions, while the laws derived from the continuous erosion studies have focused on the result and not the process of erosion. In both cases extrapolation to service conditions has been made from a limited data base and without consideration of the physical processes by which cratering occurs. Recently, attempts have been made to interrelate all aspects of the erosion process, (7) but the extensive use of empirical variables has limited the utility of this procedure for the a priori prediction of erosive material removal.

Each single particle impact causes substantial subsurface damage in addition to mass loss. (8-9) Furthermore, after many sequential single particle impacts on one specimen the average mass loss for each test is considerably higher than the base line single particle value. It has been postulated that this increase in average mass loss is due to subsurface interaction of damaged material. This increase is frequently referred to as "damage enhancement", and a damage enhancement factor has been defined



as the ratio of the mass loss obtained for a pre-damaged surface to that obtained for a virgin surface. Damage enhancement is possibly the most sensitive parameter in erosive mass loss. Experimental values of up to 3.3 have been recorded. (7) It is also a complex function of extrinsic variables (such as velocity, particle size, particle type, and temperature), as well as intrinsic variables (such as material properties and material failure modes).

The present work is directed toward quantifying the extent and nature of the subsurface damage produced by a variety of impact conditions and to assess the contribution of the most significant aspects of the subsurface damage to damage enhancement. The ultimate objective will be to suggest viable microstructural modifications that would improve the erosion resistance of carbon composites. For this purpose, detailed post-test examination of crater formation and subsurface damage have been performed for three carbon-carbon materials (Table 1) impacted by glass, nylon or water projectiles in the velocity range 1800 to 6000 ms at temperature between 20 and 3600°C. These observations have been correlated with information obtained from high speed photography, concerning the material removal sequence, and from selected quasi-static experiments, which provide ancillary data concerning both the conditions for damage formation and the physical properties of the composite constituents. These correlations permit perliminary postulates to be constructed about the details of the cratering process from initial contact to damage completion.



2.0 DAMAGE OBSERVATIONS

SC5076.4TR

The conditions used in this work for damage analysis are primarily single particle impacts produced by 1 mm glass beads using a high energy capacitor discharge exploding foil system. (4-6) The test facility can perform tests at temperatures up to 3600°C. A commercial induction heating unit is used to heat a 12 mm diameter by 12 mm long specimen to 3600°C in two to three seconds.

The craters produced at hypersonic particle impact velocities are examined using both optical and electron microscopy. Initially plan views of the craters are obtained using scanning electron microscopy to provide a general comparison of the nature of the damage from one test condition to another and for the various carbon-carbon systems. Then the crater is scanned for details of the surface fracture modes. Subsequently the specimens are sectioned. The preferred sectioning method involves impregnation of the specimen in epoxy to preserve the details of the microstructure during subsequent sectioning operations (the epoxy resin can be made to completely permeate the interior of the specimen by using a prior outgassing procedure). The section is prepared using a wire saw at the lowest possible cutting rate and then metallographically polished. Optical microscopic observations are made on progressive cross sections to establish a threedimensional picture of the extent and nature of the subsurface damage and its relation to the damage observed on the crater surface. The general nature of the damage produced for a range of conditions is summarized.

2.1 DAMAGE PERSPECTIVES

A sequence demonstrating the development of the impact damage at low temperatures (0 - 2500°C) as a function of projectile velocity (for 1 mm glass projectiles) is presented in Figure 1. At velocities below ~2000 ms⁻¹, the projectile is retained by the target (Figure 1a) and the crater consists primarily of a central zone that accommodates the penetration of the pro-



jectile. However, at higher velocities (Figure 1b), the projectile is ejected, and the crater contains an outer ledge in addition to a more deeply penetrating central zone. Surface spallation, manifested as the stripping of the lateral bundles exposed to the surface, is also apparent (Figure 1c) (longitudinal bundle is defined as a bundle oriented in the direction of the applied force, dynamic or quasi-static, -- usually the bundles normal to the surface -- while the bundles orthogonal to the applied force are referred to as lateral bundles). The sample depicted in Figure 1c was photographed prior to impact to demonstrate that the damage is localized and that no fine-scale damage occurs beyond the area encompassed by the fiber stripping boundary. An initial evaluation of the effect of microstructure (see Table 1) on the damage morphology (Figure 1c, d, e) indicates that as the proportion of longitudinal bundles increases, the central penetration zone tends to slightly increase in depth, while the outer ledge diminishes in width. Close inspection of the central zone (Figure 2a) indicates the existence of accommodation damage, manifested as exposed fibers conforming to a spherical boundary. This suggests that the central zone is formed by the direct penetration of the projectile as at the lower velocities. Kinking of the lateral fiber bundles near the crater periphery is also apparent in certain microstructures (Figure 2b), and the presence of short lengths of longitudinal fibers laterally displaced away from the impact center (Figure 2c) is commonly observed on longitudinal bundles at the crater ledge.

The damage created by deformable projectiles (water or nylon) has most of the same features (Figure 3), although there is little evidence of accommodation damage in the central zone. Also, under multiple impact conditions, linking of the outer ledge damage zones is observed at closely spaced impacts.

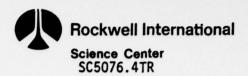
At high temperatures (> 3000°C) the impact damage is again quite similar (Figure 4), except that the impact is accompanied by permanent distortion of the fibers adjacent to the central zone (Figure 4a) and by the creation of permanent interbundle separations (Figure 4b).



2.2 DAMAGE DETAILS

The detailed nature of the impact damage has been obtained from sectioned specimens. The principal modes of damage identified in this study are summarized in schematic overviews (Figure 5a, b, c). Sections close to the center of impact obtained from low temperature impacts (< 3000°C) show that the longitudinal bundles directly beneath the central penetration zone (Figure 5a) are extensively kinked (Figure 6) and that the out-of-plane lateral bundles are ventically displaced. No clear relation between the kink mode (in or out-of-plane), the initiation site, or the location of the adjacent out-of-plane lateral bundles could be discerned (Figure 6a). Microfracture is invariably observed at the kink boundaries (Figure 6a), while independent macrofracture (Figure 6b) and partial separation of the kink boundaries (Figuse 6c) is apparent in some longitudinal bundles near the crater boundary. Several layers of in-plane lateral bundles (Figure 5b) also exhibit kinking that extends well beyond the periphery of the crater (Figure 7a). These kinks are mostly in-plane (Figure 7b, c) and generally narrower than the kinks in the longitudinal bundles. There is often a distinct fiber orientation relation (Figure 7c), position near the crater, mixed at a distance ~7d, from the center of impact (where d is the bundle thickness), and then predominatly negative at larger distances. This kinking often initiates at sites close to the corner of out-of-plane lateral fiber bundles. A more complex mode of kinking is apparent in the lateral bundles directly beneath the impact center (Figure 8). Inspection of these fiber failures indicates mixed mode kinking, usually on a plane between the opposite corners of the adjacent out-of-plane lateral bundles (Figure 8a). However, some tensile fractures (Figure 8b) and simple kinking adjacent to the matrix (Figure 8c) can also be detected.

The effects of varying the dimensions of the longitudinal bundles or the projectile velocity on the extent and morphology of the kinking are summarized in Figures 9 and 10. There is an increase in the damage extent with the projectile velocity. This is particularly prominent for the damage



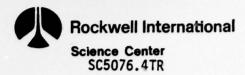
in the lateral fibers (Figure 9). However, no systematic trend in the extent of the damage zone is apparent for the various bundle configurations (Figure 9). This contrasts with some significant effects of the bundle configuration on the crater dimensions (Figure 1). The detailed morphology of the kinking in the longitudinal bundles does vary (Figure 10). For relatively large bundle diameters, the kinking is confined primarily to an intensely damaged single bundle, with some partial kinking of the adjacent bundles. For smaller bundles the kinking is usually less intense and distributed over two or more adjacent bundles.

Near the crater periphery (Figure 5c) lateral bundle fracture is typical (Figure 11a, b). Occasionally, subsurface kinks can be detected in longitudinal bundles (Figure 11c) at the lateral bundle/matrix interface. It is also apparent from the fiber configuration at the crater surface (Figure 11d) that the fractures in the longitudinal bundles that lead to material ejection are relatively planar in character and usually occur in the plane of the lateral bundle/matrix interface. Some isolated fractures in the longitudinal bundles are also evident.

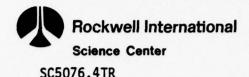
The impact damage at elevated temperatures (>3000°C) exhibit some important differences from those discerned at low temperatures. Extensive permanent distortion of the bundles near the crater surface (Figure 12) indicate that the fibers are capable of limited plastic extension prior to fracture. The kinking is less extensive, especially along the lateral bundles, and the kinks usually arrest before they propagate through the fiber bundles (Figure 12b). Fiber fracture does not invariably occur at the kink boundary (Figure 12b); rather, the kink strain is accommodated, in a significant proportion of fibers, by a permanent distortion mechanism.

2.3 MATERIAL EJECTION

High speed photographic sequences have been taken of a limited number of impacts on 2-2-3. A sequence obtained for a 1 mm glass projectile impacting at 2440 ms⁻¹, shown in Figure 13, indicates the existence of an



initial conical spray of material ejection, followed by the primary ejection phase, consisting of material ejected normal to the specimen surface as a central plume rising out of the crater. (Note that the diameter of the base of the plume is approximately equal to the particle diameter, 1 mm.) By tracing the temporal changes in the location of a distinctive feature in the plume, the approximate time at which it was freed from the crater can be reconstructed as plotted in Figure 14. It is evident that although the penetration phase was completed with <20µs, the material ejection time exceeds 200µs—over an order of magnitude longer. The primary material ejection thus occurs well after full penetration.



3.0 QUASI-STATIC STUDIES

Beside direct observations of the impact process and post-test examinations, quantitative characterization procedures were explored in order to relate the dominant failure modes to material properties. In general, conventional test procedures are not directly applicable; the strength of the composite must be considered on a scale relevant to the size of the impacting particle. The tests described here are a step in that direction. The microscopic failure modes associated with these tests are compared with those found for particle impacts as described in Section 2.0.

3.1 PENETRATION TESTS

An instrumented drop tower was used for the penetration tests (10). This test could be considered dynamic because it involves penetration velocities of a few meters per second (four orders of magnitude greater than conventional static loading rates). These tests typically last a few milliseconds, which is convenient for high temperature measurements. By directly instrumenting the penetrator, reasonably accurate simultaneous measurements of the load and deflection could be obtained. A deflection gauge system was used for penetration measurements. Two Biomation Model 802 Transient Records were used to record load and deflection signals. The records were synchronized by a Tetronix FG 501 Function Generator. The information was digitized, fed into a Hewlett-Packard Model 9830A computer, and stored on magnetic tape. The raw data could then be plotted or further processed. The final result is a plot of penetration pressure, p, versus depth of penetration q/D (normalized to the indenter diameter). A curve fitting procedure of the form

$$p = p_0 (q/D)^n \tag{1}$$

is then applied to the data. The coefficient p_o is the pressure at one diameter of penetration, while the exponent n is the slope of the pressure/penetration curve. The parameters p_o and n are determined by a least mean



squares fit. An example of this analysis is shown in Figure 15 for a penetration test on 2-2-3 material at 1000°C. Penetration pressures, p_o, obtained on 2-2-3 carbon-carbon at temperatures up to 3600°C, are plotted in Figure 16; the temperature dependence of the mass loss is also plotted for comparison. Comparing the form of the mass loss data with the penetration test results indicates that the correlation between the two damage modes is not direct, but additional thermomechanical parameters are required to establish an accurate model of the mass removal. These relations will be explored further.

The damage observed in the penetration samples is mostly similar in character to that ob cained on the impact samples, but the scale of the damage is larger (because of the larger contact area). The extended scale has the important advantage that the damage sequences can be more effectively traced, and this provides some insights into the origins of the impact damage. The damage in the longitudinal bundles has several important features (Figure 17a) that confirm inferences made from the damage in the particle impact samples. The kinking in the bundles beneath the impact crater (bundles c and d, and b, e, f below lateral bundle 3) appears to exhibit little spatial correlation, either along the bundles or between adjacent bundles. Kink pairs of opposite sign appear to be the primary mechanism for retaining the initial bundle alignment. Conversely, the kinking in the bundles beside the crater (bundles b and f) tend to exhibit a uniform spatial separation with the kinks usually initiating near the corner of an out-of-plane lateral bundle (e.g., 1b, 2b, 1f, 2f, 3f). The kink separation is thus approximately equal to the diameter of a lateral bundle plus a matrix interstice. Also, the kinks tend to conform to a single orientation. Finally, it is noted that kinks occasionally occur in bundles that are not directly subject to interaction with the penetration (e.g., bundle a).

The damage to the in-plane lateral bundles also has important implications (Figure 17b). The kinks in the bundles beside the crater are quite restricted, in marked constrast to the extensive kinking in the high velocity impact samples. These kinks are highly correlated, initiating from the corners of out-of-plane lateral fiber bundles along a single plane. It is instructive to regard these kinks as being induced by a shear displacement as depicted by the vectors in Figure 17b.

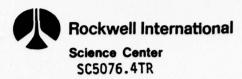


3.2 COMPLIANCE TESTS

The compliance of each zone of the composite has been evaluated using a microcompressive test. (11) The force deflection behavior indicates that the longitudinal bundles exhibit the maximum stiffness E (* 30 GPa), while the lateral fibers (in both locations) and the matrix have a similar stiffness (E = 5 GPa) at low stress levels. The greater stiffness of fiber composites in the longitudinal direction is a well-documented effect; the ratio of the lateral to longitudinal stiffness depends on the fiber loading, the matrix material, etc. (12) However, the matrix becomes nonlinear at larger stresses (due to a permanent compression associated with the porosity), and thereafter the effective tangent modulus decreases continuously with strain. The deformation characteristics of the matrix beyond yield can be assessed from a spherical indentation test, using an analysis comparable to that described for the penetration tests (Section 3.1). Then, by noting that the indentation pressure p is $~3\sigma_{_{\mathbf{V}}}$ (where $\sigma_{_{\mathbf{V}}}$ is the uniaxial flow stress), the test indicates that the initial flow stress of the matrix is -30 MPa.

3.3 PLANE-STRAIN COMPRESSION TESTS

Quantitative evaluation of the stresses required for kink formation has been achieved using a plane-strain compression test of the type illustrated schematically in Figure 18. The test entails compressing a rectangular sample (approximate dimensions 25 x 5 x 5 mm) between two parallel plattens (5 mm in width) and applying orthogonal constraints to suppress fracture. Parallelism of the plattens was achieved using a conventional hemispherical alignment fixture. The constraint was applied using horizontal miniclamps and the forces measured using strain gauges. Compression was then applied, at a constant rate of displacement, using an Instron testing machine. A typical load displacement curve is plotted in Figure 18, indicating a load instability prior to the onset of nonlinearity.



Samples tested to pre-selected loads were subsequently sectioned and metallographically polished. No permanent damage could be detected in the linear region, but kinks in one or more of the longitudinal fibers invariably could be detected after the load instability (Figure 18). The instability is thus presumed to coincide with the onset of kinking in the longitudinal fiber bundles. The kinks exhibit the same morphology (Figure 19) as those observed in the impact or penetration tests. At larger loads (Figure 18), compressional failures of the lateral bundles could be detected in the form of complex kinks between out-of-plane lateral bundles, as observed in the impacted samples (Figure 8).

The stresses in the bundles at the damage thresholds were computed by taking the applied threshold displacements and converting them into strains and then stresses, using the moduli (for the longitudinal or lateral bundles, or the matrix) computed in the compliance tests (Section 3.2). The validity of the computed stress levels was approximately substantiated by comparing the threshold stresses in the longitudinal fibers with those obtained by assuming that the load up to instability is transmitted exclusively by the longitudinal bundles (because of their much larger modulus). The threshold stresses derived in this manner for 2-2-3 are plotted in Figure 20 as a function of the constraining stresses. The threshold stress for longitudinal kinking is larger, even though it occurs at a lower applied force since the longitudinal bundles experience a substantially larger stress.

The increase in the threshold stress for longitudinal bundle kinking as the constraint is increased is approximately proportional to the level of the constraint. The result suggests a kink initiation criterion dictated by the maximum shear stress (i.e., the difference between the maximum and minimum principal stresses), as also inferred in a recent detailed study of the kink formation process. (11) In addition, under dynamic conditions there might also be a minimum stress duration for kink initiation: comparable to the incubation time for crack activation. (13)



The initiation of compressional failure in the lateral bundles does not exhibit a strong dependence on the applied constraint, suggesting a critical normal stress criterion as an approximate descriptor of damage initiation. This is again consistent with an independent analysis of the compressional damage process. (14)



4.0 DAMAGE ANALYSIS

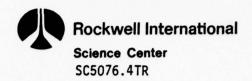
SC5076.4TR

The extent of the damage to carbon composites created by projectile impact is dictated by the stresses that develop due to the impact event and the material's resistance to the important modes of damage. Since damage can derive from both the compressive stresses (kinking) and tensile stresses (fracture), some idea of the general nature of the stresses involved in the entire impact cycle is needed to interpret the damage sequence. Then, knowledge of the conditions for initiating the various modes of damage is required in order to correlate the dynamic stresses with both the incidence of damage and material removal. A detailed analysis of this complex process can only be performed using numerical methods. However, a perspective of the process can be obtained from simplified analyses which allow elucidation of several important principles for material improvement with respect to erosive environments.

4.1 IMPACT STRESSES

Following the initial contact of the projectile and the target, a shock wave initiates and propagates away from the contact zone in both the target and the projectile. Due to the localized nature of the impact, the essentially spherical shock pulse attenuates and waves are reflected at the existing free surface and those produced during the penetration process. The cummulative wave interactions in the projectile produce significant tensile stresses. These eventually develop along the normal to the interface and the mutual contact terminates. The tensile stresses in the projectile also cause the fracture and fragmentation observed in brittle projectiles such as glass. The target material at the shock front is subjected to a hydrostatic compression.

The shock reflections at the target surface produce near-surface rarefaction waves (Figure 21). These reflected waves are the probable cause of the initial spallation damage (Figure 1c) occurring on a time scale dictated by the velocity of the attenuating shock wave. The



roughened surface of the contact zone produced by spallation will subsequently be enveloped by the sphere and carried downward during the sphere penetration stage. The presence of this roughened zone on the contact interface could produce minor perturbations in the early target/sphere interfacial pressure distribution. The sphere continues to deform as it penetrates, so the particle velocity and pressure at the actual target/sphere interface are fairly complex functions of the depth of penetration. Also the rarefaction wave developed by reflection from the target surface (as the shock wave moves outward) continues to develop, but is complicated by the presence of the crater which introduces a second free surface.

The shock related phenomena comprise only the very earliest stages of the penetration process. The expanding shock front quickly attenuates and rapidly moves out of the primary damage zone. As penetration continues the shock wave is succeeded by elastic/plastic waves (Figure 21). The term plastic wave is used here to denote the relatively slowly moving waves that encompass the non-linear zone of material response. The non-linearities could be attributed to matrix densification, matrix or fiber plasticity, or viscoelastic effects. The elastic wave generates radial compression and tangential tension with the approximate relative magnitudes depicted in Figure 21; while the plastic wave only generates compressive stresses, with the radial compression substantially larger than the tangential compression (the difference being dictated by the dynamic plastic flow stress). (15)

The penetration proceeds as the projectile decelerates, even though it may be highly fractured or extensively deformed. This process, coupled with the inertia of the expanding boundary, continues to impose a direct pressure on the surrounding material. The plastic zone continuously increases in extent during this phase.



When penetration terminates, the elastic unloading waves become fully developed. These waves can interact with the plastic waves to generate substantial tensile stresses in orientations approximately normal to the plastic wave front. (15) Material removal is typically attributed to the large tensile stresses that develop after full penetration.

These effects have been described for a target with isotropic physical properties. Local perturbations are likely for carbon-carbon composites. These would substantially modify the details of the stress magnitude and orientation (e.g., orienting the normal stresses along the bundle axis), but the sequences and modes of stress development should be essentially unchanged.

4.2 DAMAGE MECHANISMS

The character of the residual damage in impacted samples, combined with the observed material ejection sequence and the likely states of stress developed during impact, suggest the following evolution of damage. The shock wave that develops after initial contact probably leads to the formation of surface spallation (fiber stripping) due to rarefaction waves that derive from free surface reflections. The large compressive stresses at the shock front might also generate compressional failure of both the lateral bundles beneath the impact center and the lateral or longitudinal bundles adjacent to the surface (this process could also contribute to the attenuation of the shock wave). However, kinking may not be associated with the initial passage of the shock front, if the shear stresses are small. During subsequent penetration, when the shock condition is succeeded by elastic/plastic waves, compressional and shear components of stress can exist and the damage consists of both compressional bundle failure and kinking. The extention of these damage zones is dictated by the spatial and temporal details of the dynamic stress field. The damage processes are illustrated schematically (Figure 22), using possible variations in the dynamic stresses along the penetration (z) axis, with critical damage stresses superimposed. The compressional failure zone z_{max}^{c} and the kinking



zone z_{max}^k , are located by recalling that the stress (and wave speed) transmitted to the lateral bundles is lower than that transmitted along the longitudinal bundles (because of differential modulus effects) and that the stress must be applied for a minimum (incubation) time.

When penetration is complete, the tensile stresses that develop due to interaction of the unloading waves with the plastic waves are presumed to cause a portion of the damage zone to be ejected. The extent of the ejected zone depends on the residual tensile strength of the kinked material (in orientations normal to the tensile stress): a property that has not yet been adequately studied (see Figure 6c). This postulate is consistent with the primary material removal occurring well after full penetration and with the ejecta trajectories being approximately normal to the target surface (Figure 13).

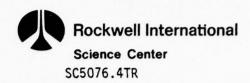


5.0 SUMMARY AND GENERAL IMPLICATIONS

The considerable differences in the extent and character of the kinking damage beneath and beside the penetration zone have important implications for the interpretation of the damage process and for designing more damage resistant materials.

Kinking of the longitudinal fiber bundles beneath the penetration zone is reproduced under dynamic and quasi-static conditions; its extent is probably dictated by the stress state near the final stages of penetration when the projectile is moving relatively slowly and the applied pressure is comparable to the quasi-static penetration pressure. The effects of the bundle dimensions and the matrix and fiber properties on the resulting impact damage should thus be related to their separate effects on the critical stress for kinking and the penetration pressure -- the latter through its influence on both the penetration distance and the dynamic stresses. It is already apparent that kinking is suppressed by increasing the matrix yield strength and elastic modulus (11) (an immediate implication for materials development). Whereas the observed lack of correlation of kinks in adjacent bundles suggests that the influence of the bundle dimensions on the kink formation condition is small. Similarly, the penetration pressure should be enhanced by increasing the matrix flow strength; while the effect of the bundle dimensions, although uncertain, is probably quite small. However, it is not immediately obvious that the extent of the kinked zone is decreased by increasing the penetration pressure. This ambiguity arises because the diminution in penetration distance is counteracted by an increase in the amplitude of the dynamic stresses. Further work is clearly needed to develop a detailed picture of the role of the penetration pressure on the extent of longitudinal fiber bundle kinking and its dependence on microstructure.

The kinking of the lateral fiber bundles beside the penetration zone is only detected under fully dynamic conditions, and its extent is strongly dependent on the impact velocity. Presumably, therefore, the conditions



that encourage this kinking develop earlier in the penetration process; perhaps because the pressure applied to the bundles declines before penetration is complete. The morphology of the kinks also suggests that the free surface has an important influence on the kinking process.

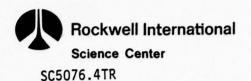
The longitudinal fiber bundles beside the penetration zone must also be damaged during the impact cycle to account for the observed occurrence of the outer ledge (Figure 1b). Since there is no systematic evidence of residual damage in these bundles, suggestions concerning the nature of this damage can only be speculative. There is much supportive evidence for the speculation that these bundles are damaged by kinking during the penetration phase and that the severity of kinking leads to the subsequent, full ejection of the damaged zone. The regularly spaced kinks (that initiate at the matrix/ bundle interface) observed adjacent to the impact center in the penetration tests, indicate that the relative displacements that accompany penetration can generate in-plane shear stresses, as indicated schematically in Figure 23. Then, the sequence of kinks required to accommodate an applied in-plane shear stress, when the restraint provided by the orthogonal bundles has been removed by prior kinking, suggests that a series of shear kinks could develop beside the penetration zone. In support of this hypothesis we note that the relatively planar character of the fractured longitudinal bundles at the base of the outer ledge is typical of kink boundary fracture, while the common occurrence of these bundle fractures at a lateral bundle/matrix interface is typical of shear induced kinks. Also, the short fiber segments sometimes observed on the longitudinal bundles, Figure 2c, could be the remnants of the kinked zone. Should this damage process pertain, the extent of the damage normal to the impact direction would exhibit (in addition to the prevading influence of the matrix flow stress and modulus) a significant dependence on the proportion of longitudinal fibers, in the sense that the damage zone will decrease as the content of longitudinal fibers increases. (11) This effect is consistent with the observations of the effect of the longitudinal fiber content on the extent of the outer ledge. It is also noted, however, that kinking of the restraining lateral bundles is a necessary precursor to the damage process; this requirement implies an upper limit on the zone size that might be encountered for relatively small longitudinal fiber contents.



Acknowledgements

SC5076.4TR

The authors appreciate the financial support provided by the Office of Naval Research under contract N00014-76-C-0854 and the funding allocated for W. F. Adler during the initial phases of this work from the Space and Missile Systems Organization contract F04701-76-C-0069 with Effects Technology, Inc. The specimens for investigation within this program were obtained from the SAMSO program and an Air Force Materials Laboratory program, contract F33615-75-C-5214, with Effects Technology, Inc.



References

- 1. R. J. Sullivan and R. R. Hockridge, "Simulation Techniques for Hypersonic Erosion Phenomena", <u>Proc. Fourth Int. Conf. on Rain Erosion and Associated Phenomena</u>, (edited by A. A. Fyall and R. B. King), published by the Royal Aircraft Establishment, England, 1974.
- 2. R. B. Mortensen, "Advanced Erosion Test Facilities", Proc. Fourth Int. Conf. on Rain Erosion and Associated Phenomena, (edited by A. A. Fyall and R. B. King), published by the Royal Aircraft Establishment, England, 1974.
- 3. W. G. Reinecke, "Rain Erosion at High Speeds", <u>Proc. Fourth Int.</u>
 <u>Conf. on Rain Erosion and Associated Phenomena</u>, (edited by A. A.

 Fyall and R. B. King), published by the Royal Aircraft Establishment,
 England, 1974.
- 4. J. D. Carlyle, M. E. Graham, and T. L. Menna, "Development of the Particle Impact Test Facility", Effects Technology, Inc. Presented at the 25th Meeting of the Aeroballistic Range Association, Naval Ordnance Laboratory, October 1974.
- 5. J. D. Carlyle, M. E. Graham, and T. L. Menna, "Particle Impact Calibration Test Results", Effects Technology, Inc. Presented at the 25th Meeting of the Aeroballistic Range Association, Naval Ordnance Laboratory, October 1974.
- J. D. Carlyle, M. E. Graham, and T. L. Menna, "Facility for High Speed Particle Impact Testing", <u>Review of Scientific Instruments</u>, 46 (1975) 1221-1225.
- 7. Effects Technology, Inc., Erosion Modeling Program, SAMSO Contract F04701-76-C-0069.
- K. Kratsch, et al., Exploratory Development and Investigation of Carbon-Carbon Composite Materials Having Improved Hypersonic Particle Erosion Resistance - CHIP (Carbon Hypersonic Impact Program), AFML-TR-75-157 (September 1975).
- 9. L. Rubin, Impact Damage Mechanisms of 3-D Carbon-Carbon Material, Space and Missile Systems Organization TR-76-142 (July 1976).
- 10. J. C. Aleszka, M. A. Ferdman, and W. F. Adler, Erosion Mechanisms Program Final Report, Volume IX, Summary of Dynamic Property Testing in Support of Erosion Model Development, Effects Technology Report No. CR77-402 (September 1977).

- A. G. Evans and W. F. Adler, "Kinking as a Mode of Structural Degradation in Carbon Fiber Composites", <u>Acta Metallurgica</u>, in press.
- 12. T. Dimmock and M. A. Abrahams, "Prediction of Composite Properties from Fiber and Matrix Properties", Composites, 1 (1969) 87-93.
- L. B. Freund, "Crack Propagation in an Elastic Solid Subjected to General Loading - III. Stress Wave Loading", J. Mech Phys. Solids, 21 (1973) 47-61.
- A. G. Evans, "A Compressional Mode of Damage in Carbon Composites", in press.
- 15. A. G. Evans, M. E. Gulden and M. Rosenblatt, "Impact Damage in Brittle Materials in the Plastic Response Regime", to be published.

Table 1. Characteristics of Carbon-Carbon Composites Investigated

MANUFACTURER		General Electric	General Electric	McDonnell Douglas
BULK DENSITY (8/cc)		1.87	1.86	1.96
UNIT CELL DIMENSIONS*	2	0.76	0.76	0.56
	Y	0.84 0.84 0.76	0.76	1.02
	×	0.84	0.76 0.76 0.76	13 1.02 1.02 0.56
NUMBER OF ENDS	7	en .	2	13
	¥	~	1 1	1
	×	7	-	7
PROCESSING		CVD + pitch	CVD + pitch	Pitch/CVD/pitch 1 1
REINFORCING FIBERS		T50	150	175
MATERIAL DESIGNATION		2-2-3	1-1-5	1-1-13

** Approximate values since billet-to-billet variations occur as well as spatial differences with a billet. * Preform dimensions for ideal conditions; not measured values from specimens examined.

FIGURE CAPTIONS

- Figure 1 Scanning electron microscope overview of craters formed by

 1 mm glass projectile impacts.
- Figure 2 Scanning electron micrographs of details of impact craters in 2-2-3 material (a) accommodation damage at the base of the central zone (b) kinking of a lateral bundle at the crater edge (c) short fiber segments on a longitudinal bundle at the outer ledge.
- Figure 3 Impact damage on 2-2-3 created by 1 mm water drops at 4000 ms⁻¹.
- Figure 4 Scanning electron micrographs of high temperature (3500°C) impact damage in 1-1-5 material impacted by a 1 mm glass projectile at 6000 ms⁻¹ indicating (a) distortion of longitudinal fibers in the central zone, (b) separation between the lateral bundles and the matrix at the outer edge.
- Figure 5 Schematics of the damage created by projectile impact (a) a section near the impact center revealing longitudinal bundles, (b) a section near the impact center revealing lateral bundles, (c) a section near the crater periphery.
- Figure 6 Optical micrographs of polished sections near the impact center revealing longitudinal bundles (a) kinking damage beneath the center of impact, (b) bundle fracture beside the crater, (c) partial separation of bundle at kink boundaries.
- Figure 7 Optical micrographs of polished sections near the impact center revealing lateral bundles (a) an overview of the kink locations, (b) a detail showing the local consistency of the kink morphology, (c) a detail showing a kink beside the crater wall.



- Figure 8 Optical micrographs of a section near the impact center showing compressional damage in lateral bundles beneath the impact zone (a) mixed mode kinks adjacent to out-of-plane lateral bundles, (b) distortion at the crater base, (c) simple kinking and fracture remote from the crater.
- Figure 9 The maximum extent of the kinking in the longitudinal and lateral bundles as a function of the projectile (1 mm glass sphere) velocity for three microstructures.
- Figure 10 Optical micrographs of sections near the impact center revealing longitudinal bundles, illustrating the effects of bundle dimensions on the kink morphology: 1 mm glass sphere impacts at 6000 ms⁻¹.
- Figure 11 Micrographs of fractures near the crater perphery (a) a scanning electron micrograph of a fractured lateral bundle,

 (b) an optical micrograph of a polished section showing a lateral bundle fracture, (c) a scanning electron micrograph of a polished section showing a sub-surface kink in a longitudinal bundle, (d) an optical micrograph of a polished section showing the morphology of the longitudinal bundle fractures.
- Figure 12 Optical micrographs of sections through a 2-2-3 material impacted at 3500°C by a glass projectile at 6000 ms⁻¹ (a) an overview showing lateral bundle distortion, (b) an overview of longitudinal bundle kinking, (d) detail of a kink in a longitudinal bundle.
- Figure 13 A high speed photographic sequence of a 1 mm glass sphere impact at 2400 ms⁻¹.

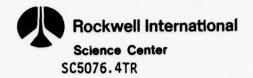
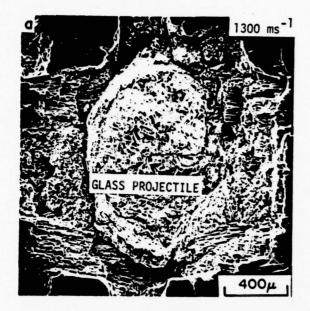
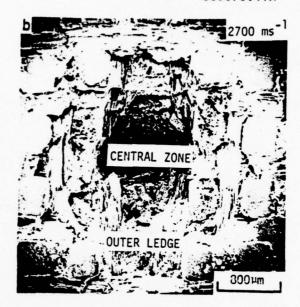
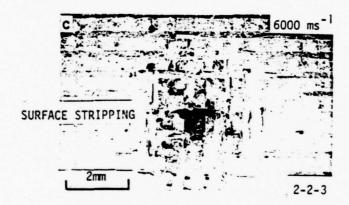


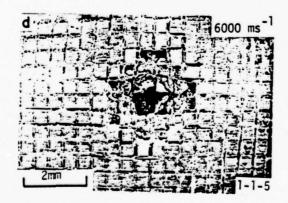
Figure 14	The temporal development of the processes accompanying a
	1 mm glass sphere impact at 2440 ms ⁻¹ .
Figure 15	The penetration pressure for 2-2-3 material at 1000°C, obtained
	using an instrumented drop weight test.
Figure 16	The temperature dependencies of the penetration pressure, po,
	and the mass loss ratio for 2-2-3 material.
Figure 17	Optical micrograph of a polished section from a drop weight
	sample of 2-2-3 revealing (a) the longitudinal bundles,
	(b) the lateral bundles beside the impact center.
Figure 18	A schematic of the plane strain compression test, and a
•	typical load, deflection curve.
Figure 19	An optical micrograph of a polished section through a compressed
	plane strain test sample revealing kinks in the longitudinal
	bundles.
Figure 20	The threshold stresses for damage formation plotted as a function
	of the lateral constraint.
Figure 21	A schematic indicating a possible sequence of dynamic stress
	development during hypervelocity impact in graphite based
	materials.
Figure 22	A schematic showing the possible temporal and spatial character
	of the principal and shear stress development along the penetration
	axis, during the projectile penetration phase, with critical
	damage formation stresses superimposed.
Figure 23	A schematic indicating the possible development of kinks in
	longitudinal bundles at the outer ledge.

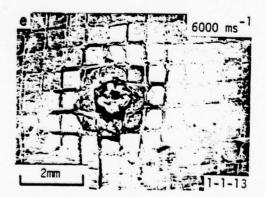




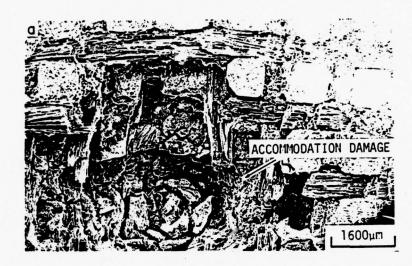














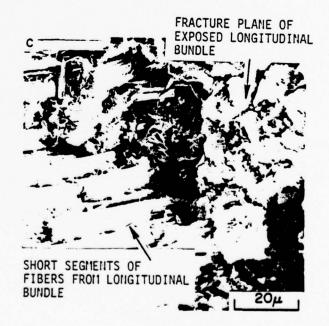


FIGURE 2





FIGURE 3





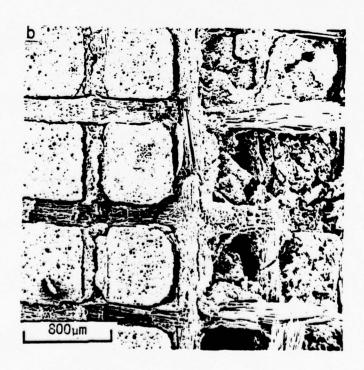
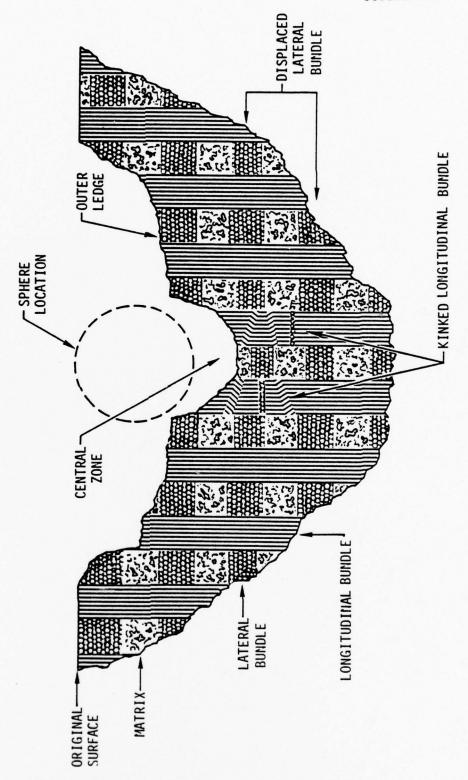
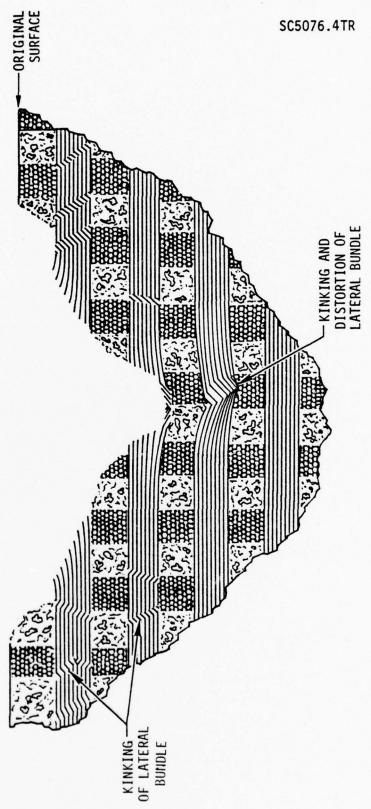


FIGURE 4

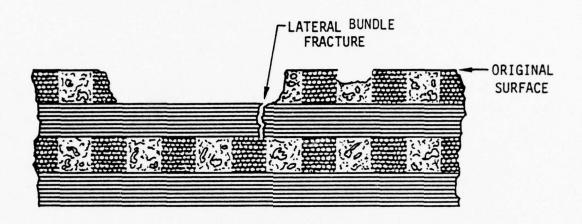


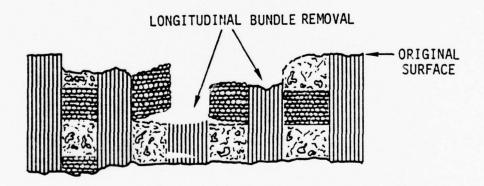






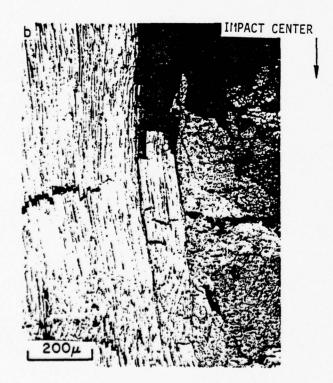












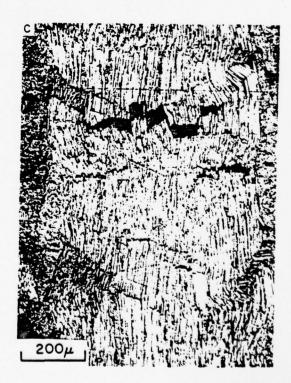
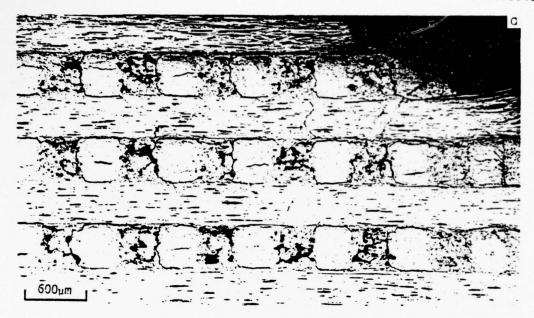


FIGURE 6





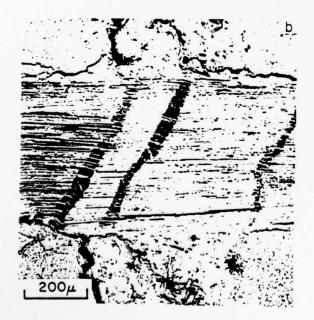
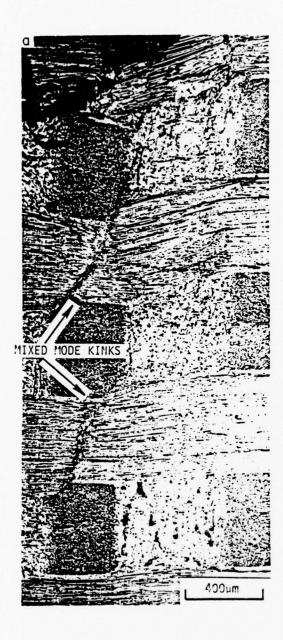
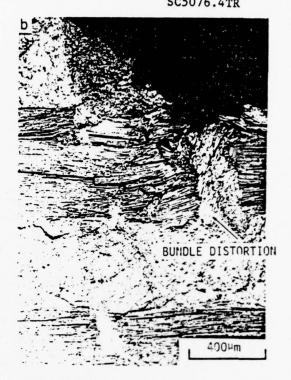




FIGURE 7







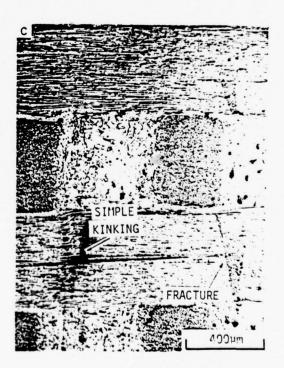


FIGURE 8



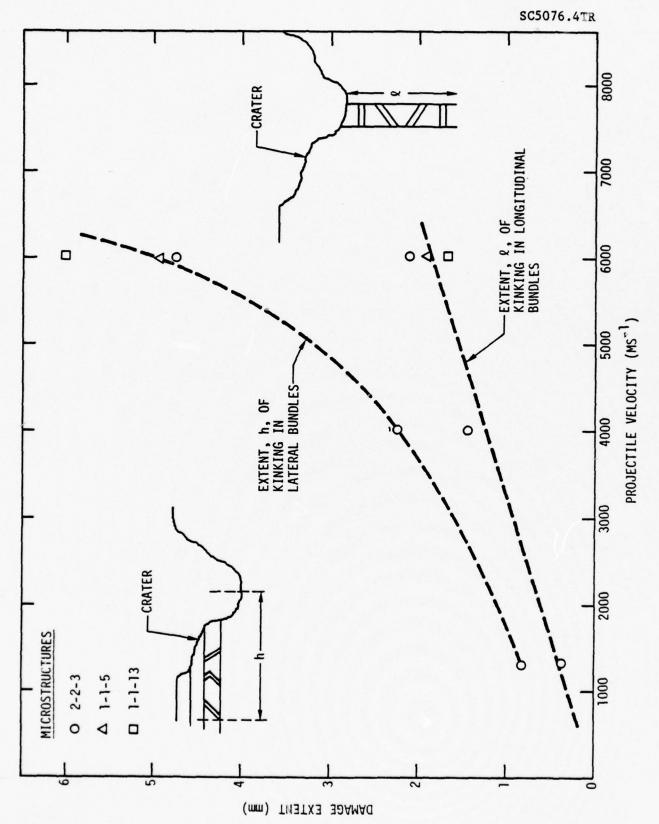
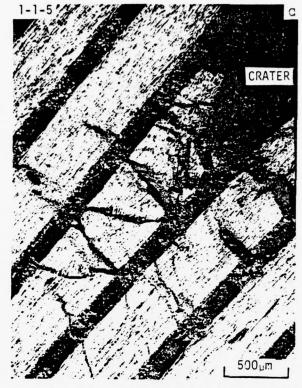


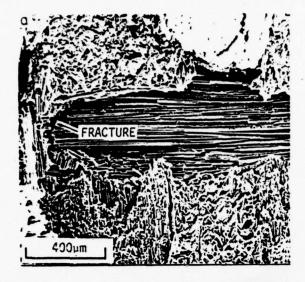
FIGURE 9





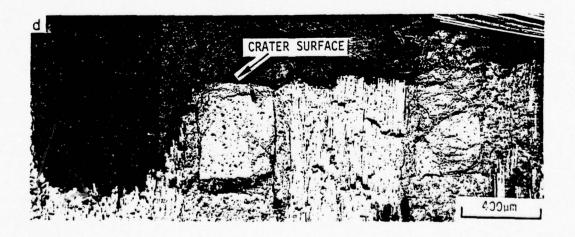














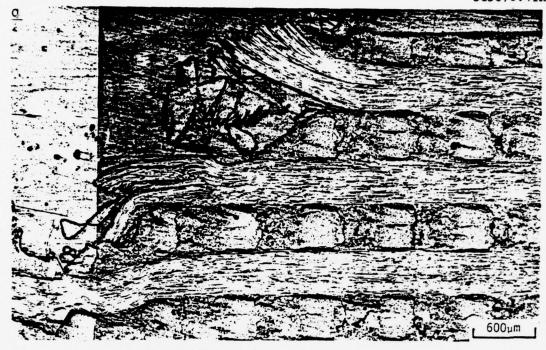






FIGURE 12



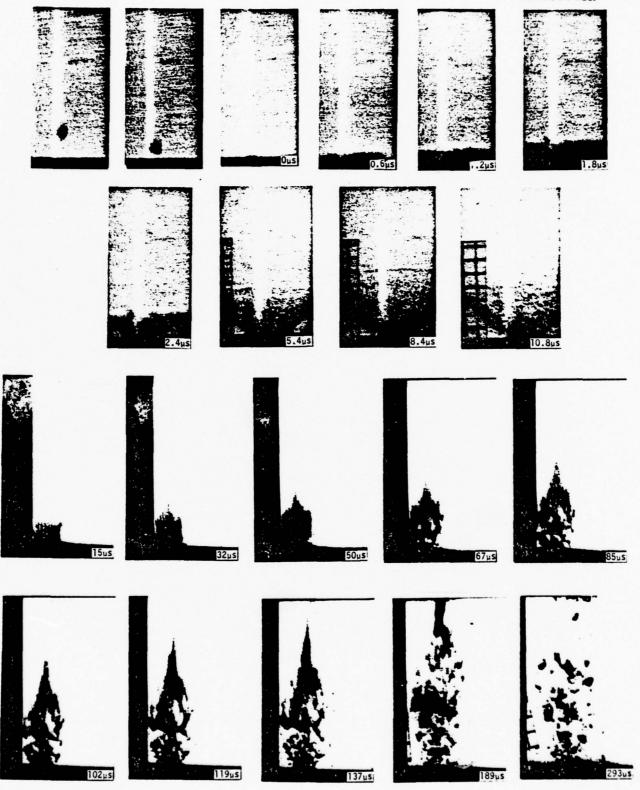


FIGURE 13



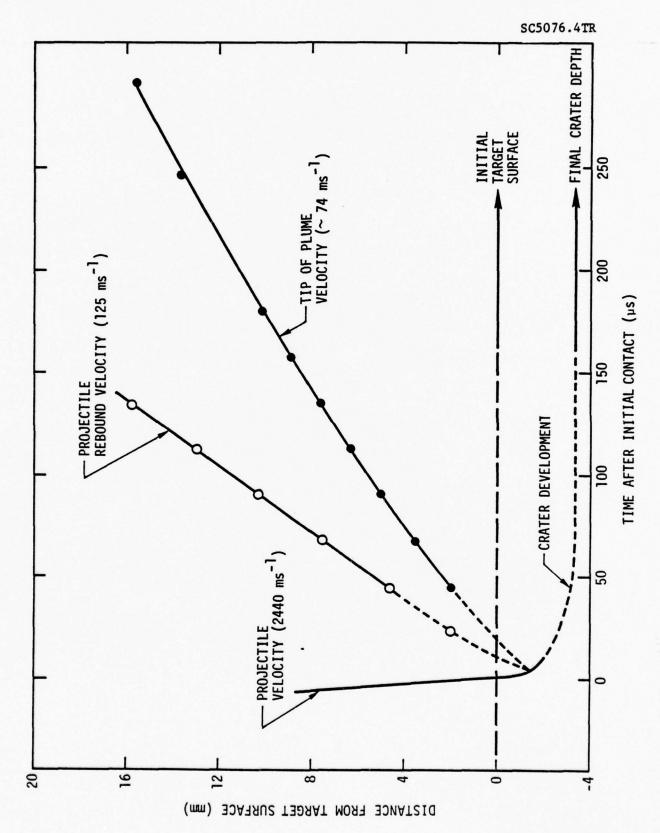


FIGURE 14



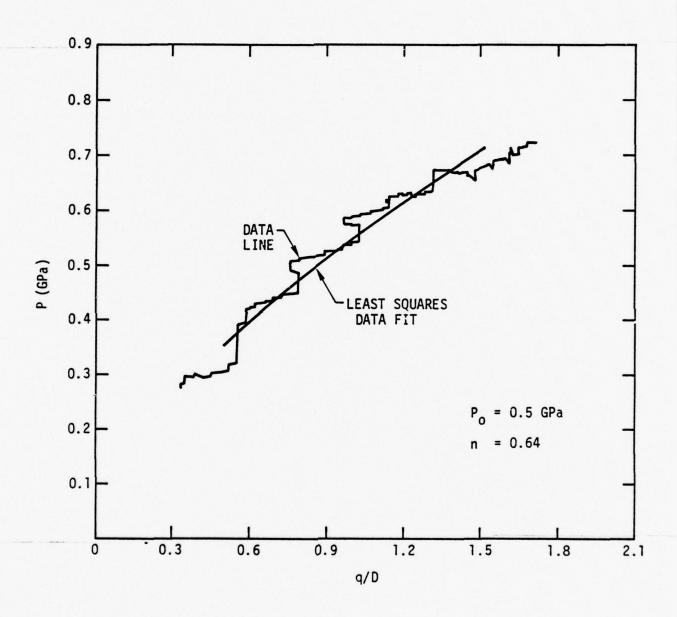


FIGURE 15



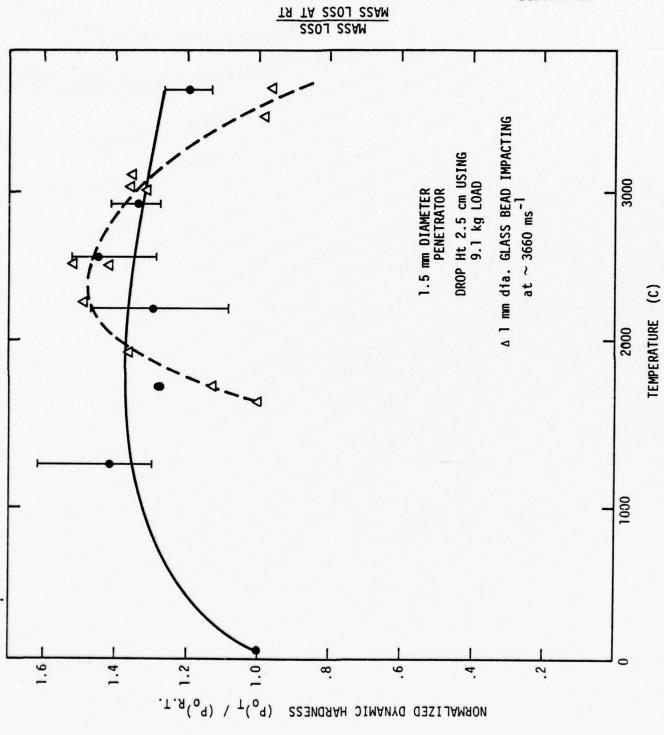


FIGURE 16

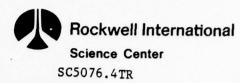
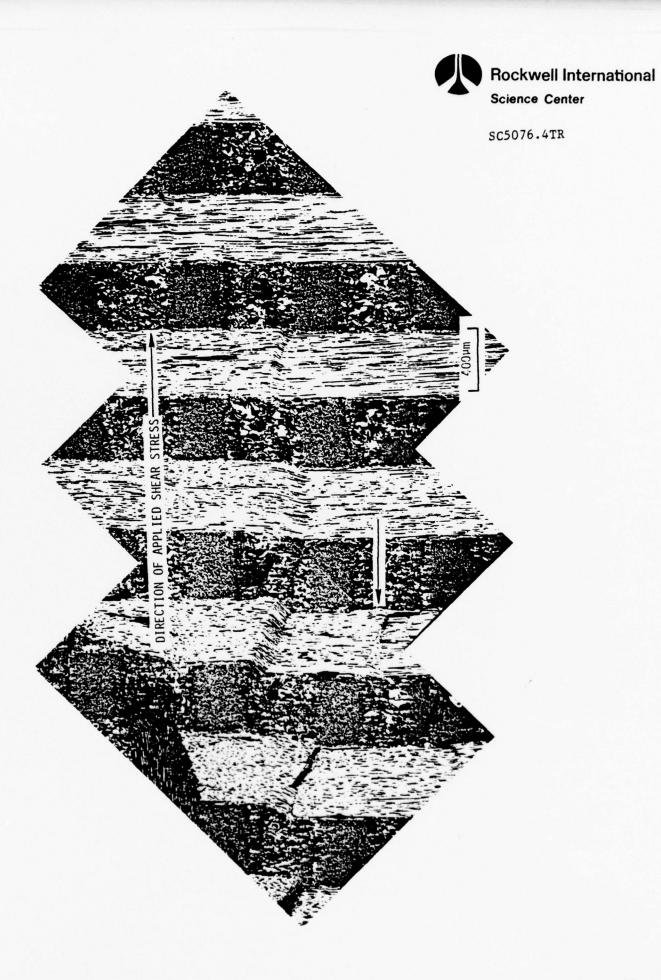
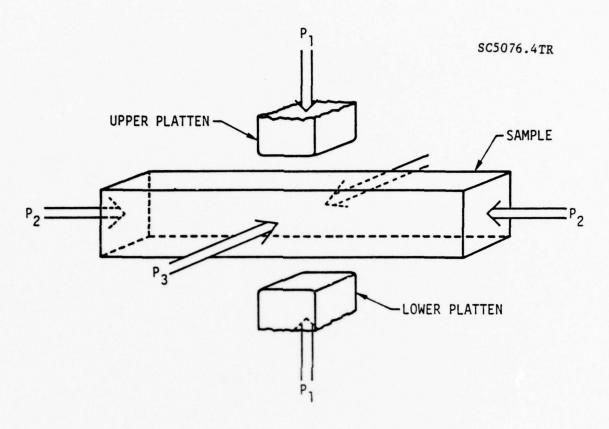




FIGURE 17







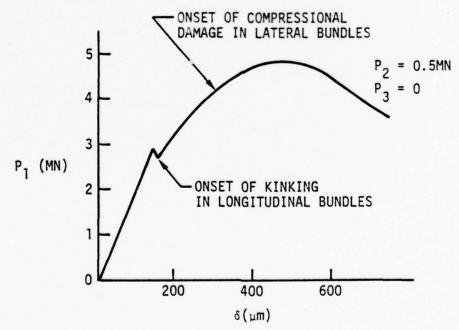


FIGURE 18



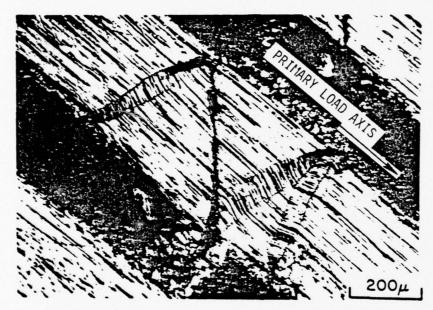


FIGURE 19



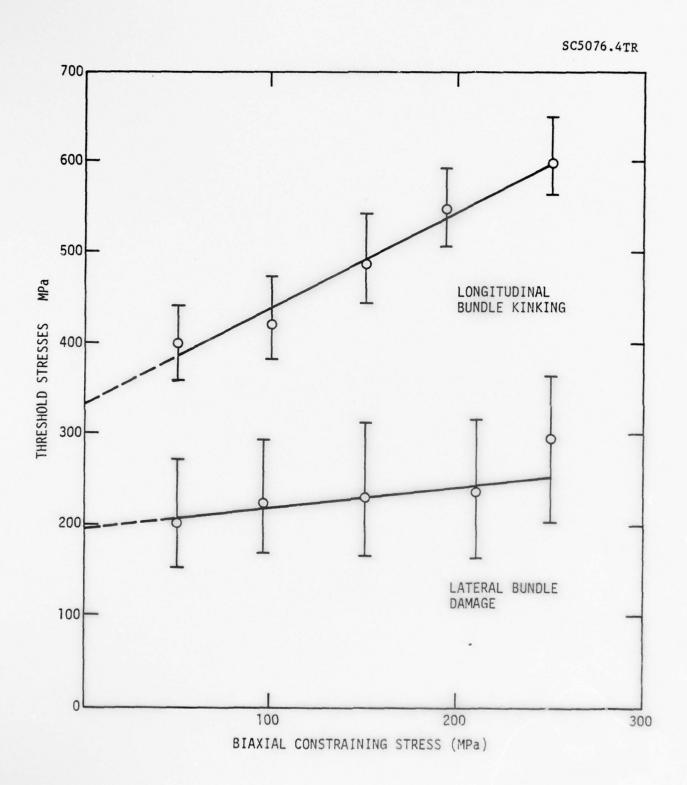
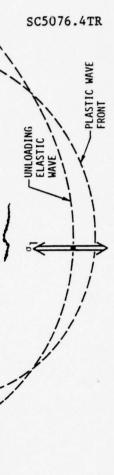
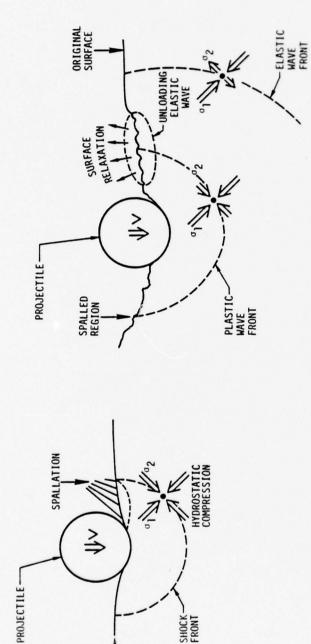


FIGURE 20







b) PARTIAL PENETRATION

a) INITIAL CONTACT

d) REBOUND

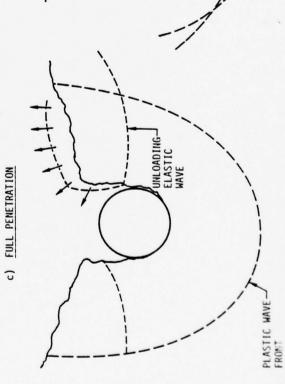
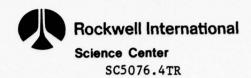


FIGURE 21

SHOCK-FRONT

SURFACE



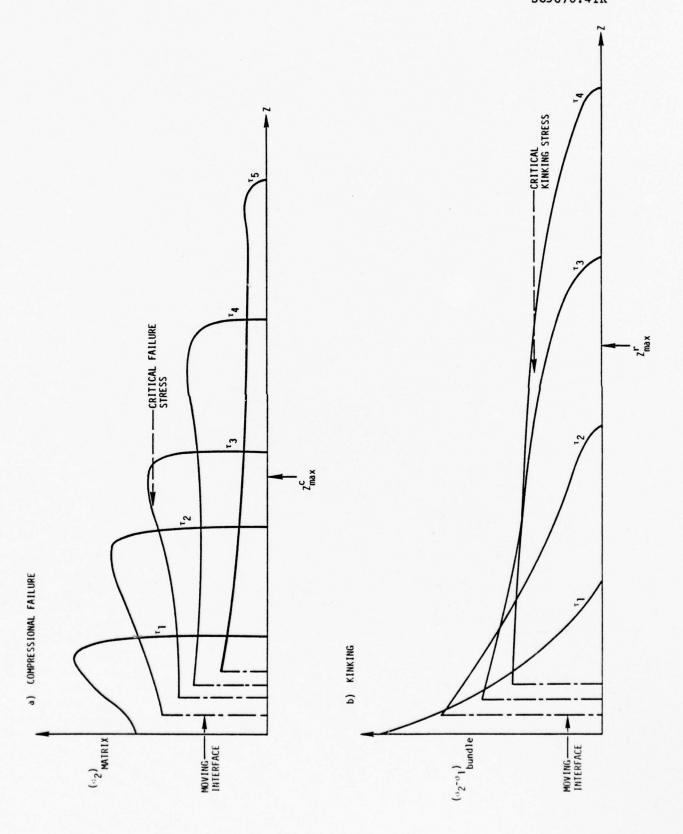


FIGURE 22



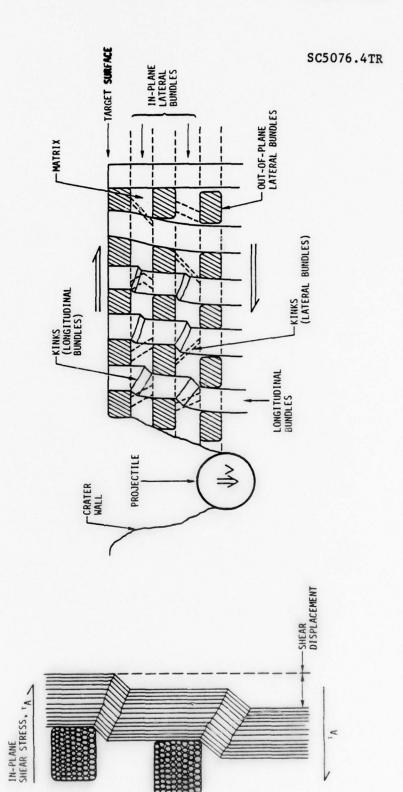


FIGURE 23



PART II

A COMPRESSIONAL MODE OF DAMAGE IN CARBON COMPOSITES

by

A. G. Evans



A COMPRESSIONAL MODE OF DAMAGE IN CARBON COMPOSITES

SC5076.4TR

A.G. Evans

Rockwell International Science Center Thousand Oaks, California 91360

ABSTRACT

One of the important modes of compressional damage in carbon composites - complex kinking of the lateral bundles - has been studied. It is shown that damage propagation is a consequence of matrix plasticity, with the damage trajectory approximately coinciding with the elastic/plastic boundary. The analysis indicates that the damage resistance is enhanced by increasing the matrix yield strength and by optimizing the relative dimensions of the bundles.



1. INTRODUCTION

Recent studies have indicated the existence of at least two modes of compressional damage in three-dimensional composites. 1,2 The more extensive damage mode is bundle kinking: the characteristics of which have been explored in a previous study. 1 The second mode is a complex fracture process 2 that occurs due to the compression of a lateral bundle between (two opposing) orthogonal lateral bundles. This damage mode is referred to as complex kinking (for reasons which will become apparent later).

The objective of this study is to identify the primary mechanism of complex kinking and thereafter, to deduce the microstructural parameters that affect its incidence. The study is part of a larger program devoted to the comprehensive characterization of the damage modes in carbon composites, as required to design microstructures with an enhanced resistance to erosion or structural degradation.²

DAMAGE OBSERVATIONS

Observations of lateral fiber damage have been made in carbon composites after either impact by small projectiles at high velocities, or quasi-static plane strain compression. Some typical damage zones are depicted in Fig. 1. The damage usually (Fig. 1a), but not always (Fig. 1b), occupies a trajectory between opposite corners of the orthogonal lateral bundles. The damage zone is usually narrow, and contains short segments of fractured fibers. The fractured fibers frequently exhibit two preferred residual orientations, especially when



the zone width exceeds the fracture length (A in Fig. la); otherwise, there are no systematic orientation effects. The orientation relations, when they exist, are reminiscent of those that prevail for kinking. This damage mode is thus referred to as complex kinking.

3. DAMAGE ANALYSIS

The bases for quantitative damage analysis are 1, a) the tensile stresses that develop in the fibers, and b) the conditions for fiber fracture. The intent of the present analysis is to develop approximate stress and fracture formulations, using simplifying assumptions where required, that permit the identification of the damage mechanism. This analysis allows several of the important parameters that control damage formation to be elucidated, and forms the basis for a subsequent, more rigorous, damage analysis.

Initially, the forces transmitted to the bundles must be related to the remote compression, σ_{∞} . These forces depend on the properties of the composite constituents. Since the overall compliance of the composite is dictated primarily by the constituent with the largest modulus, i.e. the longitudinal bundles (at least until these bundles are damaged by kinking), the stress transmitted to the lateral bundles is given by:

$$\sigma = \sigma_{\infty} \left(E_{lat} / E_{long} \right) \left(1 + d_{lat} / d_{long} \right)^{2}$$

(1)



where d is the bundle diameter, E is Young's modulus and the subscripts lat. and long. refer to the lateral and longitudinal bundles, respectively. At relatively large stress levels (beyond the interstice yield stress)

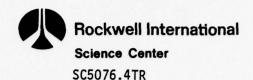
of tends to localize at the orthogonal lateral bundles. However, if the restraint provided by the longitudinal bundles is removed by kink initiation, the stress on the lateral bundles increases to,

$$\sigma = \sigma_{\infty} \left(1 + d_{lat}/d_{long}\right)^{2}$$
 (2)

The response of the fibers in the lateral bundles to the localized stress of dictates the damage. Analysis of the initial, elastic response is extremely complex if the elastic anistropies of the bundles are rigorously included. An approximate approach is thus preferred for present purposes. The simplest approximation that provides a reasonable insight into stress development within the fibers (Fig. 2) involves the estimation of the displacements in the bundle, by assuming elastic isotropy, and then uses the corresponding fiber radii of curvature to calculate the fiber stresses, by neglecting the constraint of the matrix.

The regions of maximum bundle displacement are of primary concern.

These occur near the bundle surface (Fig. 2), and can thus be obtained with sufficient accuracy by employing solutions for semi-infinite bodies subjected to surface tractions. The displacements in the horizontal direction are approximately uniform (Appendix) and do not, therefore,



contribute to fiber curvature. The approximate vertical displacements at the surface, $v_0(x)$, are;

$$v_{o}(x) \approx \frac{2\sigma}{\pi < E>} \left\{ \left[d_{\ell} - x \right] \ln \left[\frac{z^{*}}{d_{\ell} - x} \right] + x \ln(z^{*}/x) + d_{\ell} \frac{(1-\nu)}{2} \right\}$$

$$(x < d_{\ell}/2)$$

where \vee is Poisson's ratio, d_{χ} is the dimension of the pressure zone, z^* is the position of zero displacement (taken in this instance to be half the in-plane dimension of the bundle), and $\langle E \rangle$ is an average modulus for the bundle. The radii of curvature R(x) of the fibers are 3;

$$\frac{1}{R(x)} = -\frac{d^2 v_0(x)}{dx^2} = -\frac{2\sigma \left[1 - 2(x/d_{\ell})\right]}{\pi < E > x \left[1 - (x/d_{\ell})\right]}$$
(4)

The tensile stresses in the fibers are thus given approximately by;

$$\sigma_{\max} \approx E_f r_f / |R| = \frac{2\sigma(E_f / \langle E \rangle) r_f \left[1 - 2(x/d_{\ell})\right]}{\pi x \left[1 - (x/d_{\ell})\right]}$$
(5)

where σ_{\max} is the maximum tensile stress at the fiber surface, E_f is the fiber modulus and r_f the fiber radius. The stress is thus zero of the center and exhibits a singularity at the edge. The stress near the singularity will undoubtedly be modified by various relaxation effects; but we can reasonably conclude that the stress in the fibers near the edge of the loading zone will be large enough to induce fiber fracture at relatively small σ_{∞} . The extent to which the fracture propagates through



the bundle is dictated by the stress gradient. Since the stresses are a maximum along the z-axis, the displacements v(x,z) (Appendix) at small x and z are of interest. The second derivative of these displacements yields the following expression for the maximum sub-surface fiber stress

distribution;

$$\sigma_{\text{max}} \approx \frac{2\sigma \left(E_f/\langle E \rangle\right) r_f}{\pi z} \left[\ln(z^*/z) + \ln(z^*/d_{\ell}) - (1+v) \right]$$
 (6)

The principal feature to note is that the stress diminshes rapidly with distance from the surface, as $\sim z^{-1}$; reducing to values of the order of the applied pressure, σ_{∞} , at 5-10 fiber diameters. It seems improbable therefore that the damage propagation could extend beyond the first few fibers.

We will thus presume that matrix plasticity precedes substantial fiber fracture, and determine whether the consequences of plasticity are consistent with the damage observations. The zone of matrix deformation that accompanies the onset of plasticity can be approximately assessed from slip line field solutions. (It should be noted, however, that this mode of analysis implicitly assumes a plastic/rigid continuum and thus neglects elastic effects). Slip line fields derived for aligned and misaligned compression between parallel plattens are plotted in Fig. 3.

Marked similarities between the outer slip line trajectories (AOB', A'OB) and the damage zones (Fig. 1a) are immediately apparent.

These outer trajectories represent the plastic boundary, across which the tensile component of velocity is discontinuous. This discontinuity



corresponds to a zero radius of curvature for the fibers and hence, an infinite tensile stress. The magnitude of the fiber stress at the plastic boundary will, of course, be modified when elastic effects are incorporated; but the stresses are still expected to be extremely large (even for small applied displacements), and approximately invariant along the boundary.

The large magnitude and approximate constancy of the stress at the plastic boundary, and the similarity between the boundary trajectory and the observed damage zones strongly suggest that the propagation of the damage is a consequence of the onset of matrix yield. The bundle failure stress $\sigma_{\rm c}$ is thus likely to be dictated by the conditions required for matrix plasticity, derived from the slip line field solutions; 4

$$\sigma_{c} = \sigma_{y} f(h/a) \tag{7}$$

where f is plotted in Fig. 4. Combining with eqn.(1) yields the critical applied stress;

$$\sigma_{\infty c} = \sigma_{y} f(h/a) \left(E_{long} / E_{lat} \right) / \left(1 + d_{lat} / d_{long} \right)^{2}$$
 (8)

The extensive plastic flow that accompanies damage propagation will cause the broken fibers to displace plastically (Fig. 5a). Hence, when the applied stress is removed, the residual elastic strain in the fibers coupled with the constraint at the damage site (Fig. 5b) could cause a second series of fiber fractures. This type of fracture is frequently observed within the damage zone (Fig. 1).



4. DISCUSSION SC5076.4TR

The observations and analysis of lateral bundle damage contain some specific inferences about microstructural modifications that would enhance the damage resistance. The first important parameter, (as for kinking 1) is the matrix yield strength, $\sigma_{
m y}$: the critical damage stress being directly proportional to $\sigma_{\mathbf{v}}$. The relative dimensions of the lateral bundles are also important. The pressure required for matrix yield increases as h/a increases (through f(h/a)) and hence, a small ratio or the lateral dimension to the longitudinal dimension of the lateral bundles (up to 1/10) would be of significant benefit. The importance of the relative dimensions of the lateral and longitudinal bundles depends on the response of the latter. Provided that the restraint of the longitudinal bundles is intact, eqn.(8) indicates that a large proportion of longitudinal bundles is preferred. Since a large longitudinal bundle content also leads to a greater kink resistance, 1 this is a generally desirable microstructure. However, it shoud be recognized that once kinking of the longitudinal bundles initiates in a material with a large content of these bundles, extensive lateral bundle damage would quickly ensue.

The effect of an orthogonal stress applied along the axis of the lateral bundles is also of interest, especially for impact damage analysis.² In terms of the slip line field solution (Fig. 3), the orthogonal stress would supply counteracting shear stress along 45° trajectories. However, even for hydrostatic compression, shear stress would exist outside the 45° zone AQA', and damage could still occur. A relatively small dependence of the damage condition on the orthogonal stress would thus be predicted.



Appendix I

SC5076.4TR

Estimation of Bundle Displacement

The displacements at (r,θ) in a semi-infinite body subjected to a line force P per unit length are;

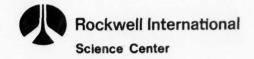
$$u = \frac{2P}{\pi < E>} \left\{ (\ell_{nr}/z^*) \cos\theta + (\ell_{nr}/z^*) \sin\theta \right\}$$

$$v = \frac{2P}{\pi < E>} \left\{ (\ell_{nr}/z^*) \sin\theta + (\ell_{nr}/z^*) \sin\theta - \frac{(\ell_{nr}/z^*)}{2} \theta \cos\theta \right\}$$
(A1)

where r and θ are the position coordinates. Expressions (A1) can be used to obtain the displacement due to a distribution of pressure, $\sigma(x)$. The horizontal displacement, u, close to the surface $(\theta^*\pi/2)$ are relatively uniform and have little effect on the stresses in the fibers. Hence, solutions are only derived for the vertical displacements, v.

Consider the displacements at a point (x,z) due to a small element d α of pressure. The vertical displacement from eqn(A1) is:

$$dv(z,x) = \frac{\sigma}{\pi < E} \qquad \left[(1+\nu)\sin\theta - (1-\nu)\theta\cos\theta + 2\sin\theta \ln(z/z \cos\theta) \right] d\alpha$$
(A2)



Integration then gives the total displacement,

$$tan^{-1} \left(\frac{d_{\chi}-x}{z}\right)$$

$$v(z,x) = \frac{\sigma z}{\pi < E^{2}} \int_{-tan^{-1}} \left\{ \left[(1+v) + 2\ln z/z^{*} \right] \frac{\sin \theta}{\cos^{2} \theta} - \frac{(1-v)\theta}{\cos \theta} - \frac{2\sin \theta}{\cos^{2} \theta} \ln \cos \theta \right\} d\theta$$

$$= \frac{\sigma}{\pi < E^{2}} \left\{ (1-v) \left[\sqrt{z^{2} + (d_{\chi}-x)^{2}} + \sqrt{z^{2} + x^{2}} \right] + 2 \sqrt{z^{2} + (d_{\chi}-x)^{2}} \ln \left(z^{*} / \sqrt{z^{2} + (d_{\chi}-x)^{2}} \right) \right. (A3)$$

$$+ 2 \sqrt{z^{2} + x^{2}} \ln \left(z^{*} / \sqrt{z^{2} + x^{2}} \right) + z (1-v) \left[\left(\frac{tan^{-1} \left(\frac{d_{\chi}-x}{z} \right)^{2} + \left(tan^{-1} \left(\frac{x}{z} \right)^{2} + \left(tan^{-1} \left(\frac{x}{z} \right)^{2} \right)^{2} + \left(tan^{-1} \left(\frac{x}{z} \right)^{2} + \left(tan^{-$$

Along the surface, z=0, this reduces to:

$$v_{o}(x) = \frac{2\sigma}{\pi < E^{>}} \left\{ (d_{\ell} - x) \ln \left[z^{*}/(d_{\ell} - x) \right] + x \ln(z^{*}/x) + d_{\ell}(1 - v)/2 \right\}$$
(A4)

ACKNOWLEDGEMENTS

The author's indebted to the Office of Naval Research for their financial support, under Contract No. N00016-76-C-0854.



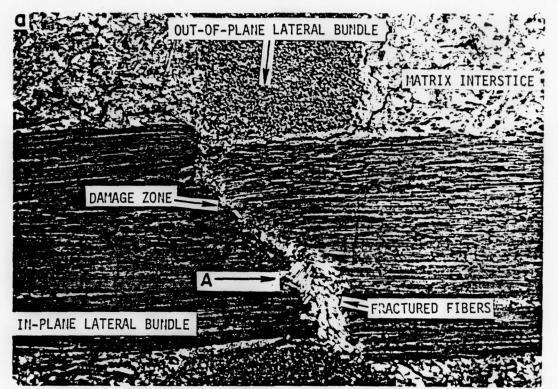
FIGURE CAPTIONS

- Figure 1. Polarized light reflected micrographs of complex kinking damage (a) a typical damage zone showing the trajectory of the damage between opposing corners of the out-of-plane bundles (b) an atypical damage zone.
- Figure 2. A schematic indicating the fiber displacement in response to the local stress σ
- Figure 3. Slip line fields for compression of a plate between plattens (a) aligned plattens (b) misaligned plattens.
- Figure 4. The indentation pressure as a function of the relative dimensions h/a of the lateral bundles.
- Figure 5. A schematic indicating a probable mode of double fracture: (a) the kink fracture when the force is applied, and the permanent plastic displacement at the damage zone; (b) the elastic relaxations and second fracture that occur at the region of high tension when the applied force is removed.



REFERENCES

- 1. A.G. Evans and W.F. Adler, Acta Met., in press.
- W.F. Adler and A.G. Evans, ASTM Special Technical Publication, in press.
- S. Timoshenko and J.M. Goodier, "Theory of Elasticity", (McGraw-Hill, New York) 1951.
- 4. R. Hill, "the Mathematical Theory of Plasticity", (Clarendon Press, Oxford), 1950.



SC5076.4TR

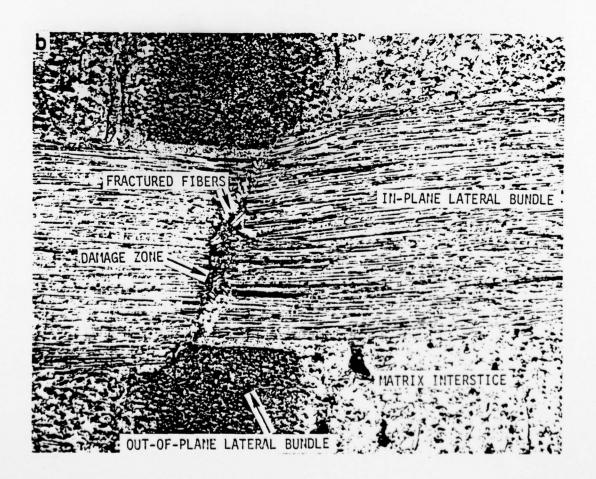
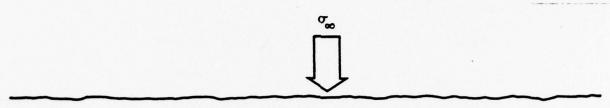


Figure 1



SC5076.4TR



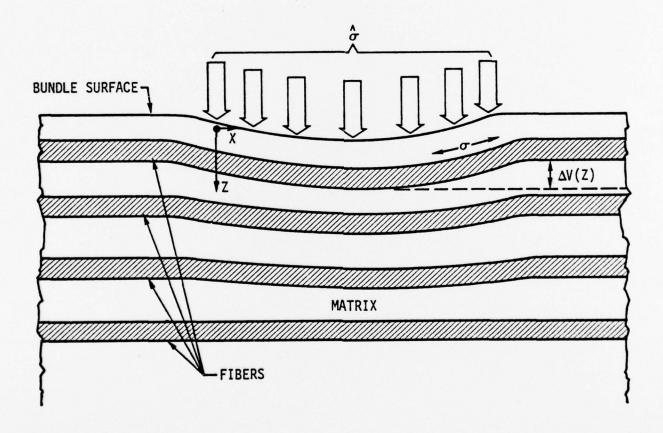
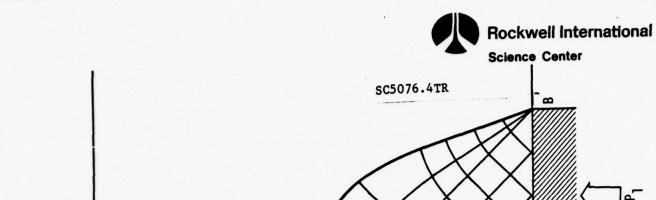
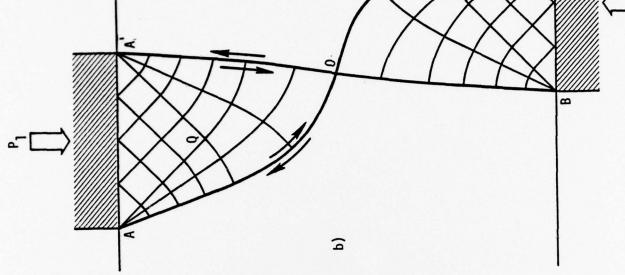
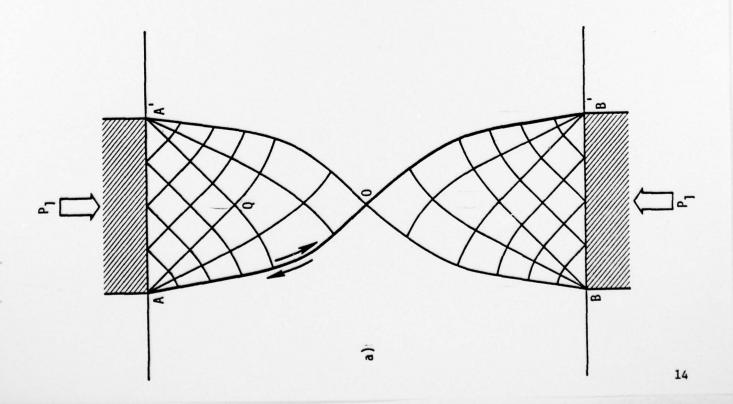


Figure 2









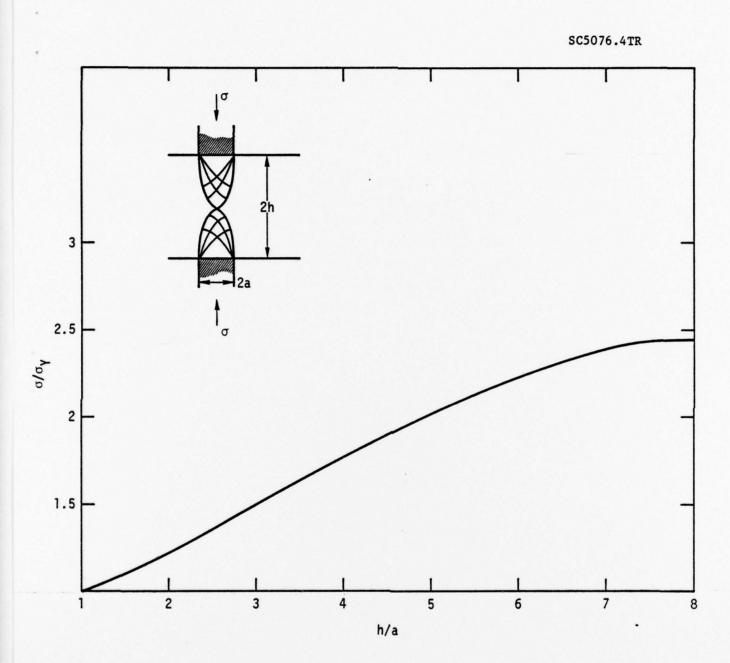
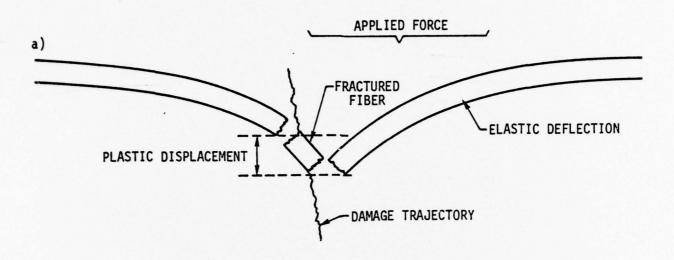


Figure 4



SC5076.4TR



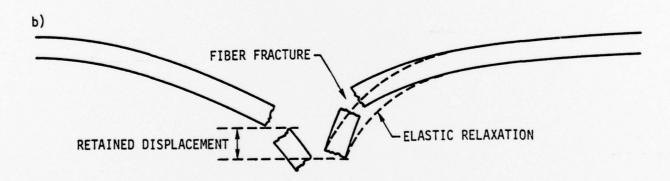


Figure 5

BASIC DISTRIBUTION LIST

October 1976

Technical and Summary Reports				
	No. of		No. of	
Organization	Copies	Organization	Copies	
Defense Documentation Center-	6	Naval Construction Batallion		
Cameron-Station-		Civil Engineering Laboratory		
Alexandria, -Virginia 22314-		Port Hueneme, California 93043		
	Cover	Attn: Materials Division	(1)	
Office of Naval Research				
Department of the Nevy Arlington, VA 22217	Shown	Naval Electronics Laboratory Center San Diego, California 92152		
Attn: -Code-471	(-) on	Attn. Electron Materials		
Code 102	(1) Cover	Sciences Division	(1)	
Code 470	(1)			
		Naval Missile Center		
Commanding Officer		Materials Consultant		
Office of Naval Research		Code 3312-1		
Branch Office		Point Mugu, California 93041	(1)	
495 Summer Street				
Boston, Massachusetts 02210	(1)	Commanding Officer		
		Naval Surface Weapons Center		
Commanding Officer		White Oak Laboratory		
Office of Naval Research		Silver Spring, Maryland 20910		
Branch Office		Attn: Library	(1)	
536 South Clark Street				
Chicago, Illinois 60605	(1)	David W. Taylor Naval Ship R&D Center	er	
		Materials Department		
Office of Naval Research		Annapolis, Maryland 21402	(1)	
San Francisco Area Office				
One Hallidie Plaza - Suite 601		Naval Undersea Center		
San Francisco, California 941	.02	San Diego, California 92132		
Attn: Dr. P. A. Miller	(1)	Attn: Library	(1)	
Naval Research Laboratory		Naval Underwater System Center		
Washington, D.C. 20390		Newport, Rhode Island 02840		
		Attn: Library	(1)	
Attn: Code 6000	(1)			
Code 6100	(1)	Naval Weapons Center		
Code 6300	(1)	China Lake, California 93555		
Code 6400	(1) Shown	Attn: Library	(1)	
-code-2627-	(-1-); -on			
	Cover	Naval Postgraduate School		
Naval Air Development Center		Monterey, California 93940		
Code 302		Attn: Mechanical Engineering Dept.	(1)	
Warminster, Pennsylvania 1897				
Attn: Mr. F. S. Williams	(1)	Naval Air Systems Command		
		Washington, D.C. 20360		
Naval Air Propulsion Test Cent	er			
Trenton, New Jersey 08628		Attn: Code 52031	(1)	
Attn: Library	(1)	Code 52032	(1)	
		Code 320	(1)	

BASIC DISTRIBUTION LIST (Cont'd)

October 1976

	No. of Copies	Organization	No. of Copies
Naval Sea Systems Command Washington, D.C. 20362 Attn: Code 035	(1)	NASA Headquarters Washington, D.C. 20546 Attn: Code RRM	(1)
Naval Facilities Engineering Command Alexandria, Virginia 22331 Attn: Code 03	(1)	NASA Lewis Research Center 21000 Brookpark Road Cleveland, Ohio 44135 Attn: Library	(1)
Scientific Advisor Commandant of the Marine Corps Washington, D.C. 20380 Attn: Code AX	(1)	National Bureau of Standards Washington, D.C. 20234	
Naval Ship Engineering Center Department of the Navy		Attn: Metallurgy Division Inorganic Materials Division	(1)
CTR BG #2 3700 East-West Highway Prince Georges Plaza Hyattsville, Maryland 20782 Attn: Engineering Materials and	(-)	Defense Metals and Ceramics Information Center Battelle Memorial Institute 505 King Avenue Columbus, Ohio 43201	(1)
Services Office, Code 6101 Army Research Office Box CM, Duke Station Durham, North Carolina 27706 Attn: Metallurgy & Ceramics Div.	(1)	Director Ordnance Research Laboratory P.O. Box 30 State College, Pennsylvania 16801	(1)
Army Materials and Mechanics Research Center Arsenal Street Watertown, Massachusetts 02172 Attn: Res. Programs Office	(1)	Director Applied Physics Laboratory University of Washington 1013 Northeast Fortieth Street Seattle, Washington 98105 Metals and Ceramics Division	(1)
(AMXMR-P) Air Force Office of Scientific Research Bldg. 410	\-\frac{1}{2}	Oak Ridge National Laboratory P.O. Box X Oak Ridge, Tennessee 37380	(1)
Bolling Air Force Base Washington, D.C. 20332 Attn: Chemical Science Directorate Electronics and Solid State Sciences Directorate	(1) (1)	Los Alamos Scientific Laboratory P.O. Box 1663 Los Alamos, New Mexico 87544 Attn: Report Librarian	(1)
Air Force Materials Lab (MX) Wright-Patterson AFB Dayton, Ohio 45433	(1)	Argonne National Laboratory Metallurgy Division P.O. Box 229 Lemont, Illinois 60439	(1)

BASIC DISTRIBUTION LIST (Cont'd)

October 1976

Organization	No. of Copies	Organization	No. of _ Copies
Brookhaven National Laboratory Technical Information Division Upton, Long Island			
New York 11973 Attn: Research Library	(1)		
Library Building 50 Room 134			
Lawrence Radiation Laboratory Berkeley, California 94720	(1)		

SUPPLEMENTARY DISTRIBUTION LIST

Technical and Summary Reports

Dr. W. F. Adler Effects Technology Inc. 5383 Hollister Avenue P.O. Box 30400 Santa Barbara, CA 92105

Dr. G. Bansal Battelle Memorial Institute 505 King Avenue Columbus, OH 43201

Dr. S. A. Bortz IITRI 10 W. 35th Street Chicago, IL 60616

Dr. J. D. Buch Prototype Development Assoc., Inc. 1740 Garry Avenue, Suite 201 Santa Ana, CA 92705

Dr. B. Budiansky
Harvard University
Department of Engineering and
Applied Science
Cambridge, MA 02138

Professor.H. Conrad University of Kentucky Materials Department Lexington, KY 40506

Dr. A. Cooper Case Western Reserve University Materials Department Cleveland, OH 44106

Dr. N. Corney
Ministry of Defence
The Adelphi
John Adam Street
London WC2N 6BB
UNITED KINGDOM

Dr. A. G. Evans Rockwell International Corporation Science Center 1049 Camino Dos Rios, P.O. Box 1085 Thousand Oaks, CA 91360

Professor John Field University of Cambridge New Cavendish Laboratory Cambridge, UNITED KINGDOM

Dr. I. Finney University of California Berkeley, CA 94720

Mr. A. A. Fyall Royal Aircraft Establishment Farnborough, Hants UNITED KINGDOM

Dr. L. M. Gillin Aeronautical Research Laboratory P.O. Box 4331 Fisherman's Bend Melbourne, VIC 3001 AUSTRALIA

Dr. M. E. Gulden International Harvester Company Solar Division 2200 Pacific Highway San Diego, CA 92138

Professor. A. H. Heuer Case Western Reserve University University Circle Cleveland, OH 44106

Dr. R. Hoaqland Battelle Memorial Institute 505 King Avenue Columbus, OH 43201

SUPPLEMENTARY DISTRIBUTION LIST (Cont'd)

Dr. R. Jaffee Electric Power Research Institute Palo Alto, CA 94300

Dr. R. N. Katz
Army Materials & Mechanics
Research Center
Watertown, MA 02171

Dr. H. Kirchner Ceramic Finishing Company P.O. Box 498 State College, PA 16801

Dr. B. Koepke Honeywell, Inc. Corporate Research Center 500 Washington Avenue, South Hopkins, MN 55343

Mr. Frank Koubek Naval Surface Weapons Center White Oak Laboratory Silver Spring, MD 20910

Dr. F. F. Lange Rockwell International Corporation Science Center 1049 Camino Dos Rios, P.O. Box 1085 Thousand Oaks, CA 91360

Dr. J. Lankford Southwest Research Institute 8500 Culebra Road San Antonio, TX 78284

Dr. B. R. Lawn
Physics Department
University New South Wales
Kingston, New South Wales
AUSTRALIA

State University of New York College of Ceramics at Alfred University ATTN: Library Alfred, NY 14802 Dr. R. E. Loehman University of Florida Ceramics Division Gainesville, FL 32601

Dr. N. MacMillan Materials Research Laboratory Pennsylvania State University College Park, PA 16802

Mr. F. Markarian Naval Weapons Center China Lake, CA 93555

Dr. F. A. McClintock Massachusetts Institute of Technology Department of Mechanical Engineering Cambridge, MA 02139

Dr. Perry A. Miles Raytheon Company Research Division 28 Seyon Street Waltham, MA 02154

Dr. D. Mulville Office of Naval Research Code 474 800 N. Quincy Street Arlington, VA 22217

Dr. N. Perrone Office of Naval Research Code 474 800 N. Quincy Street Arlington, VA 22217

Dr. J. R. Rice Brown University Division of Engineering Providence, RI 02912

Dr. R. Rice Naval Research Laboratory Code 6360 Washington, DC 20375

SUPPLEMENTARY DISTRIBUTION LIST (Cont"d)

Professor R. Roy Pennsylvania State University Materials Research Laboratory University Park, PA 16802

Dr. L. Rubin Aerospace Corporation P.O. Box 92957 Los Angeles, CA 90009

Dr. G. Schmidt Air Force Materials Laboratory Wright-Patterson AFB Dayton, OH 45433

Dr. D. A. Shockey Stanford Research Institute Poulter Laboratory Menlo Park, CA 94025

Dr. R. A. Tanzilli General Electric Company Reentry and Environmental Systems Division 3198 Chestnut Street Philadelphia, PA 19101

Dr. T. Vasilos AVCO Corporation Research and Advanced Development Division 201 Lowell Street Wilmington, MA 01887

Dr. S. M. Wiederhorn Inorganic Materials Division National Bureau of Standards Washington, DC 20234

,这种情况,我们就是一个时间,我们也是一个时间,我们也是一个时间,我们也是一个时间,我们也是一个时间,我们也是一个时间,我们也是一个时间,我们也是一个时间,我们 第一个时间,我们也是一个时间,我们是一个时间,我们是一个时间,我们也是一个时间,我们可以是一个时间,我们也是一个时间,我们也是一个时间,我们也是一个时间,我们也

ADDITIONS TO SUPPLEMENTARY DISTRIBUTION LIST

Chief, Aero & Materials Division HQ, SAMSO Los Angeles Air Force Station P.O. Box 92960 Worldway Postal Center Los Angeles, CA 90009

Dr. R. J. Drefendorf Rensselaer Polytechnic Institute Troy, NY 12181

Dr. R. Edwards NSWC - White Oak Lab. Silver Spring, MD 20910

Dr. G. Gurtman Systems, Science and Software P.O. Box 1620 La Jolla, CA 92037

Dr. Julius Jortner McDonnell Douglas Astronautics Co. Huntington Beach, CA 92647

Maj. H. Keck AFML/MXS Wright-Patterson AFB, OH 45433

Dr. W. Kessler, MBC AFML Wright-Patterson A.B, OH 45433

Dr. John F. Kincaid Strategic Systems Project Office Washington, DC 20376

Mr. Marlin Kinna Naval Sea Systems Command Arlington, VA 20362

Mr. K. Kratsch SAI 201 West Dyer Road, Unit C Santa Ana, CA 92707

Mr. K. Kreyenhager CA Research & Technology, Inc. 6269 Varlel Avenue Suite 200 Woodland Hills, CA 91367

Dr. T. McDonough Aeronautical Research Associates 50 Washington Road Princeton, NJ 08540

Mr. J. McClelland Aerospace Corporation P.O. Box 92957 Los Angeles, CA 90009

Dr. L. Peebles ONR - Boston Branch Office 495 Summer Street Boston, MA 02210

Mr. J. Persh
Office of the Director of Defense
Research and Engineering
The Pentagon
Washington, DC 20301

Mr. W. G. Reinecke AVCO Corporation 201 Lowell Street Wilmington, MA 01887

Mr. Dennis Reston
NSWC - White Oak Lab.
Silver Spring, MD 20913

Dr. W. Rosen
Materials Science Corporation
Merion Towle House
Blue Bell, PA 19422

Mr. C. Rowe NSWC - White Oak Lab. Silver Spring, MD 20910

Mr. D. L. Schmidt AFML Wright-Patterson AFB, OH 45433

Mr. R. J. Sullivan General Electric Co. REESD 3198 Chestnut Street Philadelphia, PA 19101

ADDITIONS TO SUPPLEMENTARY DISTRIBUTION LIST (CONT'D)

Dr. D. Ulrich
AFOSR/NA
Building 410
Bolling AFB
Washington, DC 20332

Dr. W. Walker AFOSR/NA Bldg 410 Bolling AFB Washington, DC 20332

Dr. I. Wollock Naval Research Laboratory Washington, DC 20375